Title

High-speed volumetric imaging of cone photoreceptors with adaptive optics spectral-domain optical coherence tomography.

Permalink

https://escholarship.org/uc/item/6rt599tv

Journal

Optics Express, 14(10)

ISSN

1094-4087

Authors

Zhang, Yan
Cense, Barry
Rha, Jungtae
et al.

Publication Date

2006-05-15

DOI

10.1364/oe.14.004380

Peer reviewed

High-speed volumetric imaging of cone photoreceptors with adaptive optics spectral-domain optical coherence tomography

Yan Zhang, Barry Cense, Jungtae Rha, Ravi S. Jonnal and Weihua Gao

School of Optometry, Indiana University, Bloomington, IN 47405
yz7@indiana.edu

Robert J. Zawadzki and John S. Werner

Vision Science and Advanced Retinal Imaging Laboratory (VSRI), Department of Ophthalmology and Vision Science,
University of California Davis,
Sacramento, CA 95817

Steve Jones and Scot Olivier

Lawrence Livermore National Laboratory, 700 East Avenue, Livermore, CA 74550

Donald T. Miller

School of Optometry, Indiana University, Bloomington, IN 47405

Abstract: We report the first observations of the three-dimensional morphology of cone photoreceptors in the living human retina. Images were acquired with a high-speed adaptive optics (AO) spectral-domain optical coherence tomography (SD-OCT) camera. The AO system consisted of a Shack-Hartmann wavefront sensor and bimorph mirror (AOptix) that measured and corrected the ocular and system aberrations at a closed-loop rate of 12 Hz. The bimorph mirror was positioned between the XY mechanical scanners and the subject's eye. The SD-OCT system consisted of a superluminescent diode and a 512 pixel line scan charge-coupled device (CCD) that acquired 75,000 A-scans/s. This rate is more than two times faster than that previously reported. Retinal motion artifacts were minimized by quickly acquiring small volume images of the retina with and without AO compensation. Camera sensitivity was sufficient to detect reflections from all major retinal layers. The regular distribution of bright spots observed within C-scans at the inner segment / outer segment (IS/OS) junctions and at the posterior tips of the OS were found to be highly correlated with one another and with the expected cone spacing. No correlation was found between the posterior tips of the OS and the other retinal layers examined, including the retinal pigment epithelium.

References and links

1. D. Huang, E. A. Swanson, C. P. Lin, J. S. Schuman, W. G. Stinson, W. Chang, M. R. Hee, T. Flotte, K. Gregory, C. Puliafito, J. G. Fujimoto, "Optical coherence tomography," Science **254**, 1178-81 (1991).
2. A. F. Fercher, C. K. Hitzenberger, G. Kamp, Y. Elzaiat, "Measurement of intraocular distance by backscattering spectral interferometry," Opt. Commun. **117**, 43-48 (1995).

3. M., Wojtkowski, R. A. Leitgeb, A. Kowalczyk, T. Bajraszewski and A. F. Fercher, "In vivo human retinal imaging by Fourier domain optical coherence tomography," J. Biomed. Opt. **7**, 457-463 (2002).
4. B. Cense, N. A. Nassif, T. C. Chen, M. C. Pierce, S. Yun, B. H. Park, B. E. Bouma, G. J. Tearney, and J. F. de Boer, "Ultrahigh-resolution high-speed retinal imaging using spectral-domain optical coherence tomography," Opt. Express **12**, 2435-2447 (2004).
5. M. Wojtkowski, V. J. Srinivasan, T. H. Ko, J. G. Fujimoto, A. Kowalczyk, and J. S. Duker, "Ultrahigh-resolution, high-speed, Fourier domain optical coherence tomography and methods for dispersion compensation," Opt. Express **12**, 2404-2421 (2004).
6. R. A. Leitgeb, W. Drexler, A. Unterhuber, B. Hermann, T. Bajraszewski, T. Le, A. Stingl, and A. F. Fercher, "Ultrahigh resolution Fourier domain optical coherence tomography," Opt. Express **12**, 2156-2165 (2004).
7. J. Liang, D. Williams, and D. Miller, "Supernormal vision and high-resolution retinal imaging through adaptive optics," J. Opt. Soc. Am. A **11,** 2884-2892 (1997).
8. A. Roorda, F. Romero-Borja, W. J. Donnelly, H. Queener, T. J. Hebert, and M. C. W. Campbell, "Adaptive optics scanning laser ophthalmoscopy," Optics Express **10**, 405-412 (2002).
9. N. Doble, G. Yoon, L. Chen, P. Bierden, B. Singer, S. Olivier, and D. R. Williams, "Use of a microelectromechanical mirror for adaptive optics in the human eye," Opt. Lett. **27**, 1537-1539 (2002).
10. M. Glanc, E. Gendron, F. Lacombe, D. Lafaille, J. F. Le Gargasson, and P. Lena, "Towards wide-field imaging with adaptive optics," Opt. Commun. **230**, 225-238 (2004).
11. J. Rha, K. E. Thorn, R. S. Jonnal, J. Qu, Y. Zhang, and D. T. Miller, "Adaptive optics flood-illumination camera for high speed retinal imaging," Opt. Express (accepted).
12. Y. Zhang, J. Rha, R. S. Jonnal, and D. T. Miller, "Adaptive optics parallel spectral domain optical coherence tomography for imaging the living retina," Opt. Express **13**, 4792-4811 (2005).
13 R. J. Zawadzki, S. M. Jones, S. S. Olivier, M. Zhao, B. A. Bower, J. A. Izatt, S. Choi, S. Laut, and J. S. Werner, "Adaptive-optics optical coherence tomography for high-resolution and high-speed 3D retinal in vivo imaging," Opt. Express **13**, 8532-8546 (2005).
14. E. J. Fernández, B. Považay, B. Hermann, A. Unterhuber, H. Sattmann, P. M. Prieto, R. Leitgeb, P. Ahnelt, P. Artal and W. Drexler, "Three-dimensional adaptive Optics ultrahigh-resolution optical coherence tomography using a liquid crystal spatial light modulator," Vision Res. **45**, 3432-3444 (2005).
15. L. A. Riggs and J. C. Armington, J. C., "Motions of the retinal image during fixation," J. Opt. Soc. Am. A **44**, 315-321 (1954).
16. American National Standard for the Safe Use of Lasers ANSI Z136.1. (Laser Institute of America, Orlando, FL, 2000).
17. C. A. Curcio, K. R. Sloan, R. E. Kalina, and A. E. Hendrickson, "Human photoreceptor topography," J. Comparitive Neurology **292**, 497-523 (1990).
18. D. R. Williams, "Topography of the foveal cone mosaic in the living human eye," Vision Res. **28**, 433-454 (1988).
19. D. H. Anderson and S. K. Fisher, "The relationship of primate foveal cones to the pigment epithelium," J. Ultrastructure Res. **67**, 23-32 (1979).
20. R. H. Steinberg, I. Wood, and M. J. Hogan, "Pigment epithelial ensheathment and phagogytosis of extrafoveal cones in human retina," Philos. Trans. R. Soc. London. **277**, 459-474 (1977).
21. E. Götzinger, M. Pircher, and C. K. Hitzenberger, "High speed spectral domain polarization sensitive optical coherence tomography of the human retina," Opt. Express **13**, 10217-10229 (2005).

1. Introduction

Optical coherence tomography (OCT) is a leading modality for non-invasive, *in vivo* imaging of the human retina, providing unprecedented sensitivity and axial resolution [1-2]. Recent development of spectral domain optical coherence tomography (SD-OCT) has led to substantial gains in image acquisition speed without loss in sensitivity and resolution, a performance achievement not possible with conventional time-domain optical coherence tomography [3-6]. High sensitivity, axial resolution, and speed are important instrument attributes for probing the retina at the cellular level, a research area that has attracted much attention owing to its potential to quantify visual function and retinal pathology of individual cells. An additional important attribute, however, is high lateral resolution. The lateral resolution of OCT in the eye is poor – typically reported at no better than 15 μm - due to a small imaging pupil (<2mm) and the presence of ocular aberrations.

For fundus cameras and scanning laser ophthalmoscopes, lateral resolution has been substantially increased, approaching 2 μm, by imaging through a large pupil and correcting the ocular aberrations with AO [7-11]. These cameras, however, exhibit noticeably poorer

axial resolution than OCT (more than an order of magnitude) due to the low numerical aperture (NA) of the eye (even when dilated) and are unable to create volume images of the retina with a 3D resolution that is comparable to the size of individual cells.

Given the complementary strengths of AO and SD-OCT, a resolution approaching a few microns in all three dimensions is possible with their combination. To date, AO has been combined with free space parallel SD-OCT [12] and fiber based SD-OCT [13-14]. These instruments have been reported to achieve lateral and axial resolutions up to 3 μm and 2-3 μm in the eye, respectively. The instruments, however, were tailored for specific experiments that did not emphasize volumetric imaging of single cells. For example, the AO free space parallel SD-OCT successfully acquired B-scans that showed individual cone photoreceptors resolved in both axial and lateral dimensions. The instrument could not capture volume images though as it had no mechanism to laterally scan the line illumination and detector across the retina. The AO fiber based SD-OCT instruments successfully acquired volume images. One of the instruments [13] obtained B-scans of sufficient quality to reveal individual cone photoreceptors. For volume imaging, however, the long exposure durations (<6 s for a volume image), the saw-tooth scan pattern, and the large scanning range (1.67x0.67 deg) exposed the volume images to substantial retina motion artifacts that seriously compromised observation of cone photoreceptors in extracted C-scans.

To address these limitations, we have developed an AO fiber based SD-OCT retina camera that acquires A-scans faster (75,000 /s), raster scans over a shorter distance (38 A-scans per B-scan), and employs a symmetric triangular scan pattern that reduces the time delay between consecutive B-scans. Collectively, these permit small rectangular retinal patches $38 \times 19 \times 1100$ μm (width× length×depth) to be imaged in <10 ms, a time duration that is short enough to freeze the motion of the retina in a fixating eye [11,15]. Larger volume images up to $38 \times 285 \times 1100$ μm were imaged in <150 ms, a time duration that results in some motion artifacts, but nevertheless substantially less than that in previously reported AO-OCT volume images. In this paper, we evaluate the sensitivity of the AO SD-OCT camera, acquire volume retinal images on two subjects, compare C-scan images at different depths and eccentricities in the retina, and quantify changes in the retinal reflectance caused by compensation of ocular aberrations. The resolution, sensitivity, and acquisition rate of the camera were found sufficient for imaging the three-dimensional morphology of cone photoreceptors in both subjects.

2. Methods

2.1. Adaptive optics spectral domain optical coherence tomography

The AO SD-OCT camera consisted of three channels: (1) sample channel, equipped with AO, for collecting the retinal reflection, (2) reference channel with an optical path length matching that of the sample channel, and (3) detection channel for recording the combined spectrally-encoded sample and reference signatures. The layout of the camera is shown in Fig. 1 and described below.

The illumination source for the AO SD-OCT camera was a 10 mW broadband superluminescent diode (SLD) ($\lambda = 842$ nm, $\Delta\lambda = 50$ nm). In the sample channel, the SLD light exiting the fiber propagated through five relay telescopes consisting of ten spherical mirrors with protected silver coating. The pupil of the eye was conjugated to the wavefront corrector (an AOptix deformable mirror), the two scanning mirrors, the 20×20 lenslet array (f=30mm, lenslet diameter = 500μm) of the Shack-Hartmann wavefront sensor (SHWS), and a circular aperture positioned immediately after the collimation optic for the SLD. The AO system was incorporated into the sample channel and operated simultaneously with the SD-OCT system. A 90/10 pellicle was inserted after the system stop to redirect 10% of the light reflected from the eye to the SHWS. The lenslet array sampled the wavefront across a 6.6 mm pupil of eye. The array of focal spots produced by this lenslet array was recorded with a Dalsa

1M60 CCD camera. Displacements of the spots compared to a preset reference were fed into a direct slope control algorithm to be rapidly converted to control voltages for the AOptix mirror. The AO system could perform up to 30 wavefront measurements and corrections per second, although the typical rate during the experiment was 12 Hz due to signal-to-noise (SNR) required of the SHWS. The AOptix bimorph had 37 actuators with a maximum displacement (stroke) of 32 µm for defocus correction.
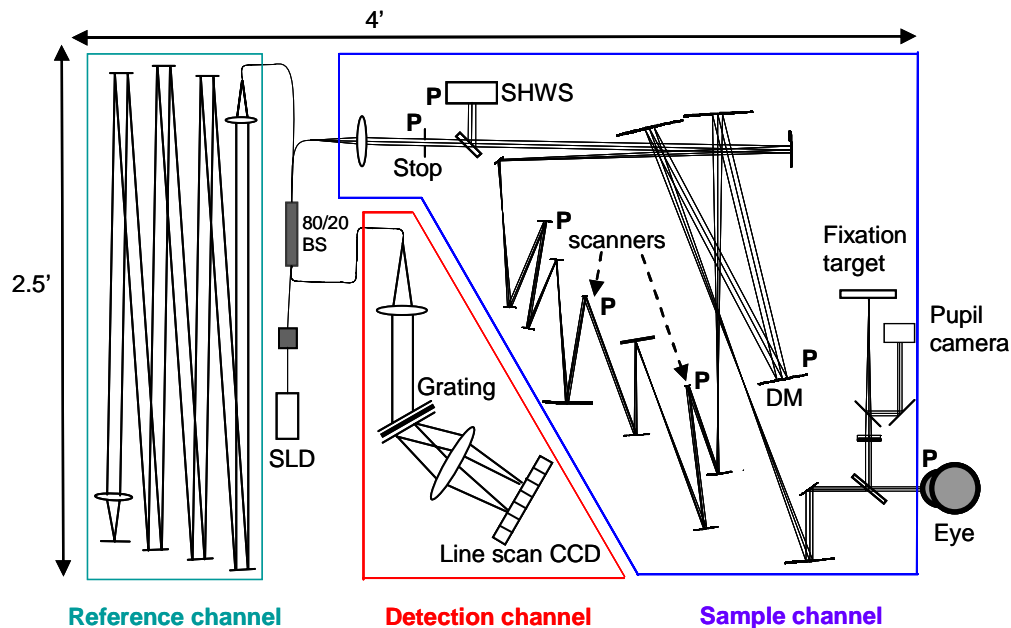

Fig. 1. Layout of the AO SD-OCT retina camera. The camera consists of three channels: (1) sample channel, (2) reference channel, and (3) detection channel. The AO system is integrated into the sample channel. BS, DM, and P refer to the fiber beam splitter, AOptix deformable mirror, and planes that are conjugate to the pupil of the eye, respectively.

The large stroke is highly attractive for retinal imaging as it permits compensation of relatively large amounts of sphere and cylinder refractive error, thereby obviating the need for trial lenses or at least the meticulous use of such lenses. Such relatively large corrections, however, were found to present unexpected challenges for the system design. For example, analysis of our initial AO SD-OCT design, which is consistent with the practice in the field, with commercial ray tracing software (Zemax, Inc.) revealed that mirror correction of defocus (sphere) and astigmatism (cylinder) generates noticeable beam distortion at the pupil of the eye when the bimorph mirror is placed between the SLD light source and XY scanners. Similarly, large uncorrected refractive errors of the subject generate noticeable beam distortion at the mirror and the SHWS. This sequential arrangement of light source, wavefront corrector and scanners has been exclusively used for integrating AO into both the SLO [8] and scanning OCT [13-14] instruments. Our ray tracing predicted that the distortion increases with the magnitude of the mirror correction (or equivalently with the refractive error of the subject), the reflection angle at the spherical mirrors in the relay telescopes, and the f/# of the mirrors. For our AO-OCT design, mirror half angles were not unusual with values ranging from 5 to 10 degrees and many being around 7.5 degrees. f/# of the spherical mirrors ranged from 18 to 37. Beam distortion at the pupil reduces resolution in one dimension and causes vignetting in the other. To illustrate, Fig. 2(a) shows the outcome of a Zemax ray trace simulation for the original AO-OCT design. Shown is the shape of the beam entering the pupil of the eye when

the radius of curvature of the bimorph mirror is set to compensate 0 and ±3 diopters of defocus. For the ±3 diopter cases, the beam shape is noticeably oval with the short axis roughly half that of the other axis. For the 0 diopter case, the beam is approximately circular.

To overcome this difficulty and regain effective use of the full mirror stroke, we discovered that strategic placement of the bimorph mirror very close to the eye, i.e., one relay telescope away from the eye, (see Fig. 1) yielded essentially no beam distortion, as shown in Fig. 2(b). In this arrangement, the mirror lies between the scanners and eye. This arrangement is effective because it minimizes the propagation of the mirror compensation through the system. With the direction of light reversed, it also minimizes the propagation of ocular refractive errors through the system prior to compensation. The final AO-OCT design (shown in Fig. 1) occupied roughly the same footprint, and contained the same approximate range of mirror half angles and f/# of the spherical mirrors as that of the original design. While our analysis of these two specific designs is too narrow to generalize to other systems, it does reveal the importance of checking for pupil distortion in this type of instrument when using a deformable mirror with large stroke.

In the reference channel, light was collimated by a microscope objective lens (10X) and propagated between six planar mirrors with protected silver coating. The reference beam was then focused onto the 7th planar mirror by a thin singlet plano-convex lens and reflected back to the fiber. A water vial was placed in the beam path to compensate chromatic dispersion induced by the eye. The overall optical path length was set to match that of the sample channel (4.7m).
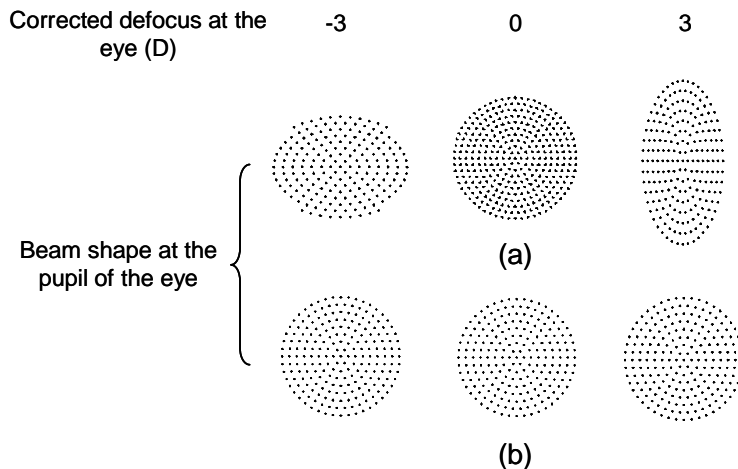

Fig. 2. Predicted shape of the beam entering the eye for a range of refractive corrections by the wavefront corrector in the (a) original and (b) final AO-OCT designs. Refractive corrections are 0 (middle) and ±3 (left, right) diopters across a 6.6 mm pupil. The two designs are described in the text with the final one shown in Fig. 1.

Light from the sample and reference channels were combined using an 80/20 fiber coupler. Light exiting the fiber coupler in the detection channel was collimated by an achromat doublet lens (f=75mm) and diffracted by a 1,200 lines/mm transmission grating (Wasatch Photonics) at Littrow's angle. Grating efficiency for the first order was 86% at 830 nm. A multi-element photographic lens focused light on a line-scan CCD detector (12 bit, 512 pixels Atmel). Note that a buffer limitation on the frame grabber that controls the linescan camera caused approximately every 19th B-scan to be dropped. This created some loss of spatial information (~5%), although it did not hinder analysis of the images. Custom software was developed to

acquire raw spectral images, subtract reference spectra, interpolate into *k*-space, balance dispersion, Fourier transform, and finally display the reconstructed volumetric retinal images. Exposure level at the cornea was at most 430 μW and complied with the American National Standards Institute (ANSI) [16].

2.2. Human subjects

AO SD-OCT images were collected on two subjects that were free of ocular disease and had normal corrected vision. Both subjects were mildly myopic (-2.5 diopter sphere; -1.5 diopter sphere × 1.5 diopter cylinder). The subject's line of sight was centered along the optical axis of the retina camera with the aid of a fixation target, bite-bar stage, and video camera that monitored the subject's pupil in retro-illumination. The fixation target was located at the subject's far field and consisted of high contrast cross hairs positioned on a rectilinear grid 1 degree apart. The target was back illuminated with uniform red light. As shown in Fig. 1, the target was positioned in the sample channel such that its view was not affected by the AO. A dental impression attached to a sturdy xyz bite-bar translation stage stabilized the subject's head and provided accurate pupil positioning. A 50/50 pellicle was placed in front of the fixation target, splitting part of the reflected beam from the eye and redirecting it to the pupil camera, as shown in Fig. 1. Retro-illumination of the pupil was realized with the same 842 nm SLD.

The subjects were mildly cyclopleged and their pupils dilated using two drops of Tropicamide 1% that were administered prior to measurements and one drop every hour thereafter. A single drop of Phenylephrine Hydrochloride 2.5% was also applied at the beginning of the measurements for additional dilation.

Refractive errors of sphere (defocus) and cylinder (astigmatism) were coarsely reduced by insertion of trial lenses at the spectacle plane. The remaining defocus and astigmatism were corrected with the AO system. The trial lenses were slightly tilted to divert their strong reflections.

2.3. OCT sensitivity

Prior to retinal imaging, the sensitivity of the SD-OCT system was measured by substituting a model eye consisting of an achromatic lens and planar mirror in the sample channel [4]. A neutral density filter placed in the reference channel limited the reference beam intensity to one quarter (49,485 electrons) of the CCD pixel well depth capacity (197,940 electrons), similar to the sample beam intensity. One thousand CCD frames of the reference beam were captured and averaged. Then, interference spectra were recorded as the optical path length of the reference channel was incremented in 200 μm steps via a one-dimensional stage. Measurements were acquired over a 1.2 mm range, equivalent to 0.87 mm in retinal tissue (assuming an aggregate refractive index, n_{retina}, of 1.38). For each step, reconstructed B-scans were used to determine the experimental sensitivity. To calculate the theoretical sensitivity, the optical power of the light reflected from the model eye was also measured at the fiber coupler's input end of the detection channel by a power meter (Newport, Inc.). The power incident on the model eye was 430 μW, integration time of the CCD line scan was 20 μs, and the detection channel efficiency was measured at 21%. The full-width-half-height (FWHH) of the axial point spread function (PSF) was also measured and converted to that in retinal tissue, again, assuming 1.38 for n_{retina}.

2.4. Retinal imaging

Small patches of retina 38×285×1100 μm (width×length×depth) were imaged within a time duration of 150 ms and with a sampling density of 1×1×2.2 μm. While retina motion artifacts such as image distortion will be present across the entire volume image, laterally small 38 μm × 19 μm sub-sections of the volume image should be essentially free of motion artifacts as these are acquired within 10 ms. As an additional pre-cautionary step, B-scans were

automatically registered in both lateral and axial dimensions using a customized cross-correlation algorithm. This further reduced any distortions that might have been present in the final volume images. The slow scan employed a saw-toothed pattern that cycled at 6.7 Hz; the fast scan used a symmetric triangular pattern that cycled at 1.0 KHz. In both subjects, volume retinal images were acquired with and without dynamic AO correction and at retinal eccentricities of 1°, 2°, 3°, and 7° (superior retina). At each retinal location, focus was adjusted by $1/6^{th}$ diopter (~60 μm) steps in order to optimize cone photoreceptor clarity. Focusing was realized with the AO system [13].

3. Results and discussion

3.1. OCT sensitivity and axial resolution

Figure 3 shows measured sensitivity as a function of depth. Sensitivity peaks at 91 dB, which is in good agreement with the theoretical value of 95 dB. The figure also shows an 8 dB/mm sensitivity drop, due to limitations of the detection channel, in particular, the undersampling of interference fringes at high frequencies. Imaging depth in air is 1.5 mm, equivalent to 1.1 mm in tissue. The theoretical full width at half height (FWHH) axial resolution (= $2\ln2/\pi$ * $\lambda_o^2/\Delta\lambda n_{retina}$) in retinal tissue for the 842 nm SLD is 4.5 μm. The measured resolution obtained with the model eye is 6.6 μm (air), which corresponds to 4.8 μm in the retina. The difference between theoretical and experimental values is likely due to residual dispersion mismatch, a non-Gaussian spectral shape, and non-linearity in the optics.
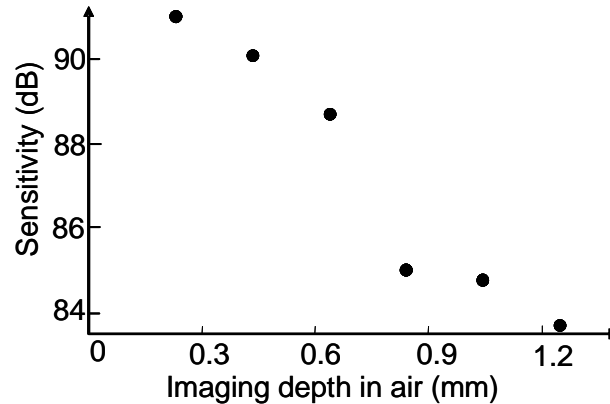

Fig. 3. OCT sensitivity as a function of depth in air. A drop in sensitivity of 8 dB/mm was measured.

3.2. AO performance

Figure 4(a) shows the measured wave aberrations across a 6.6 mm pupil for one of the subjects before and during dynamic AO correction. AO compensation clearly reduces the magnitude of the aberrations and increases the Strehl ratio at the SLD wavelength of 842nm from 7% to 35%. As an alternative image quality metric, Fig. 4(b) shows a root mean square (RMS) trace of the measured wave aberrations for the same subject before and during AO dynamic correction. Once initiated, full correction is achieved in a few iterations of the AO loop and typically reaches a mean corrected RMS of about 0.12 μm. For the second subject, AO reduced the RMS error of the wavefront from 0.66 to 0.13 μm. These results were found highly repeatable throughout the experiment for both subjects.

Measured aberrated
wavefront

AO-OFF

Strehl Ratio=7%
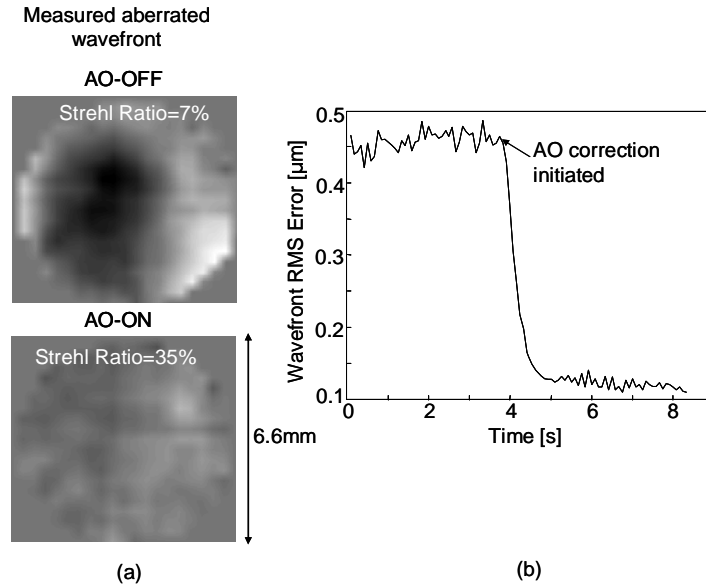
AO-ON

Strehl Ratio=35%

6.6mm

(a)

(b)

Fig. 4 (a) Residual wave aberrations across a 6.6 mm pupil in one subject as measured by the SHWS before and after AO compensation. Wavefront phase is represented by a gray-scale image with black and white tones depicting minimum (-1.0 μm) and maximum (1.19 μm) phase, respectively. (b) An RMS trace of the residual wave aberrations is shown for one subject before and during dynamic AO correction.

3.3. Volumetric imaging

Figure 5 shows two representative AO-OCT volume images acquired with a sampling density of $1\times1\times2.2$ μm at 1° and 7° retinal eccentricity on one subject. Focus lies in the vicinity of the photoreceptor layer, i.e. the focus position that provided the sharpest images of cone photoreceptor structure using focus adjustments of $1/6^{th}$ diopters. Theoretical depth of focus is about 50 μm and is defined as two times the Rayleigh range for a Gaussian beam and a 6.6 mm pupil. The figure illustrates that even at the high acquisition rate of 75,000 A-scans/s, camera sensitivity remains sufficient for visualizing all major retinal layers, including the external limiting membrane (ELM). The brightest reflections occur within the photoreceptor and retinal pigment epithelium (RPE) layers, which are at the bottom of the 3D visualization.

To better assess the presence of retinal microstructure in the volume image at 1° eccentricity, Fig. 6 shows the volume as a movie sequence of C-scan images. A B-scan through the volume (average of 3 B-scans) is also shown to indicate C-scan depth. The video is shown duplicated using log and linear intensity scales, the motivation for both being as follows. While a log scale is used almost exclusively for displaying OCT images of the retina in order to emphasize weakly reflecting tissue (e.g., inner and outer plexiform and nuclear layers), this is at the expense of reduced display contrast for highly reflective tissue (e.g., photoreceptors and RPE). It is not surprising then that images of cone photoreceptors acquired with AO fundus cameras and AO SLOs are routinely displayed on a linear scale. The use of log and linear scales in Fig. 6 therefore facilitates comparison to OCT, fundus camera, and cSLO images of the retina.
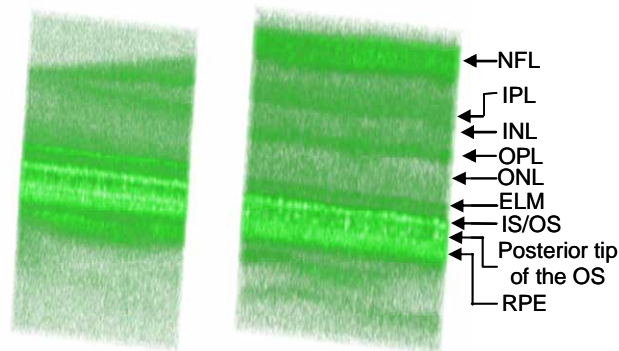
Fig. 5. (2.8 MB) Movie presenting 3D visualization of a small patch of retina at (left) 1° and (right) 7° retinal eccentricity in one subject. Volume images were acquired with AO compensation and focus at the photoreceptor layer. The retinal volume is 38×190×495 μm (width×length×depth). Volume images were acquired within 100 ms and are displayed using an intensity log scale (2.8 MB version).

The C-scan videos reveal the same stratified layers of the retina that are apparent in the Fig. 5 3D visualizations. Microscopic details in the volumes, however, are more clearly discernible in the C-scans. Unfortunately, high contrast speckle is a prominent microscopic feature in many of the layers and masks retinal information, especially retinal detail approaching the size of individual speckle. Speckle in the AO SD-OCT images is roughly the average size predicted by theory (2.6 and 4.7 μm in width and depth, respectively) for the imaging configuration used here. That is, the lateral dimension is given by the diffraction-limited spot size and the axial dimension by the OCT resolution. For much of the retina, a more serious masking effect is defocus. This is especially true for the anterior portion of the retinal image as it falls noticeably outside the depth of focus (50 μm), which is located about the photoreceptor layer.

Within the depth of focus, speckle noise is less obtrusive. Reflections near the interface between the inner and outer segments of the photoreceptors (IS/OS) as well as the distal tips of the photoreceptors, just above the RPE, appear as a quasi-regular pattern of bright spots in the C-scans. Periodicity of the pattern is several microns. Note that the pattern is more discernible in the linear intensity video. At least qualitatively, this pattern appears similar to that reported with AO fundus cameras and cSLOs when focused on the photoreceptor layer. Initial observation suggests that the bright spot pattern is distinctively different from the reflective pattern shown at other depths, such as the RPE layer.

As another example, Fig. 7 shows C-scans extracted from volume images at 2° eccentricity for both subjects. As in Fig. 6, the Fig. 7 C-scans are largely dominated by high frequency irregular structure that is suggestive of speckle. Speckle again appears less obtrusive at the IS/OS junctions and posterior tips of the OS where a regular array of bright spots is observed. While one might expect a similar regular pattern to occur at the ELM as the inner segments of the photoreceptors terminate there, we were unable to discern one. This might be because light reflected at the ELM is not waveguided given that it presumably does not enter the inner segment. Another possibility is the noticeably lower signal to noise at this interface that may be too low for detecting this pattern and therefore our failure to observe one.
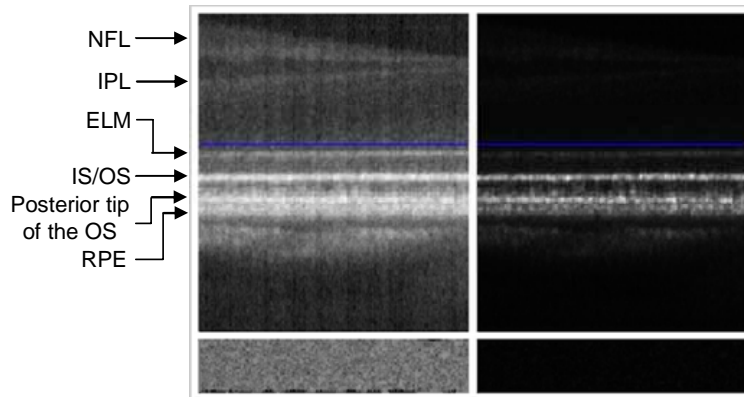
Fig. 6. (2.4 Mb) Movie sequence of C-scans extracted from the volume image at 1° eccentricity in Fig. 5. To indicate C-scan depth, a representative B-scan (average of 3 B-scans) with a blue indicator line is also shown. The video is shown twice using (left) log and (right) linear intensity scales in order to facilitate visualization of both bright and dim retinal structures. Focus is approximately at the plane of the photoreceptors. C-scans are 38 μm × 190 μm. (2.4 MB version).
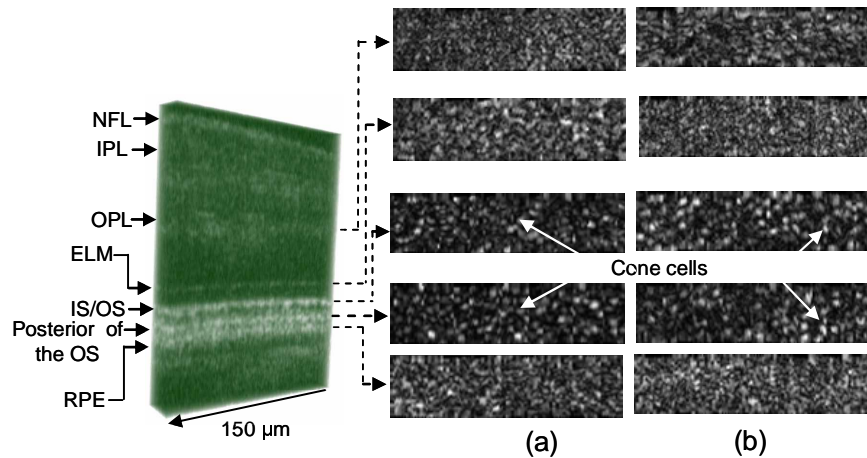
Fig. 7. C-scans extracted from several depths in AO-OCT volume images that were acquired at 2° eccentricity on (a) subject RJ (b) subject DTM. C-scans correspond to the OPL, ELM, IS/OS junction, posterior of OS, and RPE. Focus is approximately at the plane of the photoreceptors. Images are displayed using a linear intensity scale. C-scans are 38 μm × 150 μm and were acquired in <80 ms.

While the pattern of bright spots is qualitatively similar to that of cone photoreceptors imaged with AO fundus and cSLO cameras, a more quantitative assessment is to compare spot spacing to known cone spacing estimated from histology and psychophysical observations. To this end, the center-to-center spacing of bright spots was measured manually in AO-OCT images acquired at 1°, 2°, and 3° eccentricity for both subjects and 7° for the one subject in which images were collected at this eccentricity. Care was taken to avoid regions in the images that showed motion distortion and B-scan dropout. Representative C-scan images at the posterior tips of OS are shown in Fig. 8 for both subjects. Note the gradual increase in spacing with eccentricity with the spot density highest at 1° and lowest at 7°. As cones are largely arranged in a hexagonal matrix, their fundamental frequency is inversely related to the

spacing of cone rows (= center-to-center spacing * cos30°). As such, average spacing of the spots was transformed to row spacing and then plotted in Fig. 9 along with estimates from histology and psychophysical observations [17, 18]. The plot shows that spacing of the bright spots agrees well with the estimates of cone spacing for 1°, 2°, and 3° eccentricity and roughly for 7°. The strong agreement at 1°, 2°, and 3° and the consistent trend up through 7° supports the view that the observed bright spot pattern at the posterior tip of the OS is indeed reflections from the cone photoreceptors.
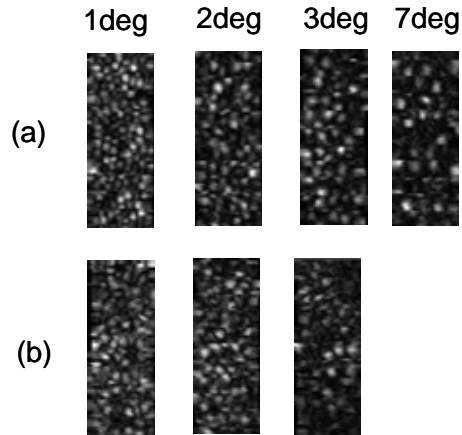

Fig. 8. C-scan images at the posterior tips of OS acquired in (a) one subject at 1, 2, 3, 7 degree eccentricity and (b) another subject at 1, 2, 3 degree eccentricity. C-scan images are 38x100 μm subsections of the original images and were acquired in <60 ms. Focus is approximately at the plane of the photoreceptors. Images are displayed using a linear intensity scale.
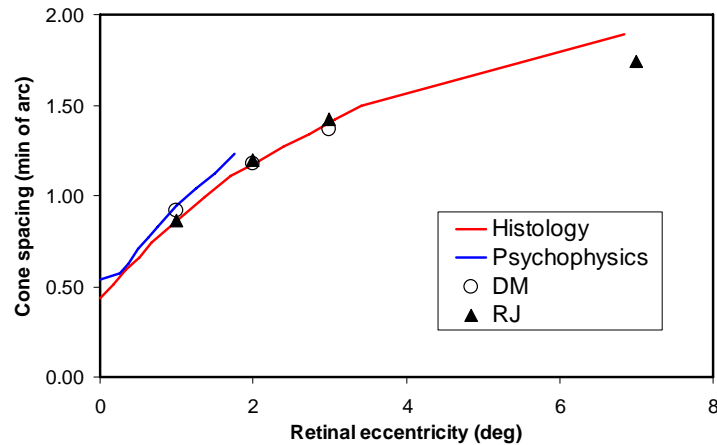

Fig. 9. Row spacing of bright spots at the posteriors tips of OS in AO SD-OCT C-scans as a function of retinal eccentricity. Cone row spacing is also shown as estimated from histology (superior and inferior retina) and psychophysical observations of aliasing with interference fringes [17,18].

One visually striking feature in the volume retinal images of Figs. 6 and 7 is the apparent similarity in the pattern of bright spots at the IS/OS junctions and that at the posterior tips of the OS. To quantify this observation, the cross correlation was computed between C-scans at these two depths as well as between the posterior tips of the OS and several other layers (OPL,

ELM, and RPE). The resulting correlation maps between the posterior tips of the OS and IS/OS junctions and RPE are shown in Fig. 10. Central peak correlation values at all retinal eccentricities and depths, and for both subjects are listed in Table 1. Indeed Fig. 10 and Table 1 confirm a strong correlation between the reflections at the IS/OS junctions and posterior tips of the OS. This suggests that both reflections are waveguided by the photoreceptor optics and further strengthens the common belief that the photoreceptor outer segment acts as a fiber-like structure. It also suggests that the inner segment has fiber-like properties. Interestingly this strong correlation was found only between these two layers. This is strong evidence that the waveguided light that reflects back out of cone photoreceptors (as routinely observed with AO fundus cameras and AO scanning laser ophthalmoscopes) originates from only two narrow layers that straddle the OS. We found no evidence that the light reflected from the RPE was recaptured by the overlying cone photoreceptors.
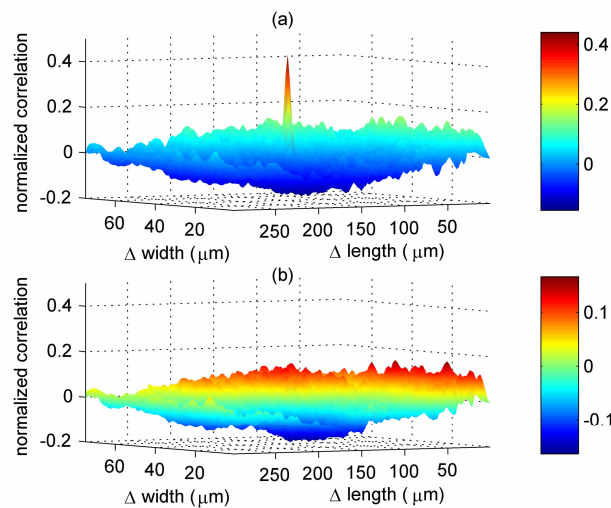

Fig. 10. Cross correlation between C-scans at the posterior tip of OS and (a) IS/OS junction and (b) RPE in the same subject. The cross correlation was computed using the Matlab 7.0 (Mathworks, Inc.) function "normxcorr2."

Strong correlation between the IS/OS junctions and the posterior tips of the OS was found at all retinal eccentricities and in both subjects examined. While the IS/OS junctions of both rod and cone photoreceptors lie at the same proximal depth, the posterior tips of their outer segments lie at distinctly different depths. Namely, the posterior tips of the cones are ensheathed by an RPE apical process that typically extends 10 to 20 µm from the RPE cell, a separation that is dependent on retinal eccentricity [19-20]. Rods on the other hand have longer outer segments with posterior tips that embed directly into the RPE cell. In this paper, the label coined the posterior tips of the OS (e.g., Fig. 8) refers to what we believe to be that of cone photoreceptors, not rod photoreceptors. Thus reflections at this retinal depth should be void of any rod reflection and for that matter any RPE reflection. The fact that a strong correlation was observed between this layer and the IS/OS junctions at 7° (where rods are more numerous than cones) indicates that rods contribute noticeably less to the IS/OS junction reflections than cones. Had the rod reflection been bright, one would expect a distribution at the IS/OS junction markedly different from that at the posterior tips, which would have led to a drastic reduction of the central peak value of the cross correlation between the two corresponding C-scans.

Note that the bright reflective layer we have interpreted as the posterior tips of the OS is consistent with polarization sensitive measurements of the retina [21]. Specifically, this bright

layer was found to largely preserve the incident polarization, while the immediate underlying tissue layer scrambled it. This result coupled with the scattering property of RPE cells suggest the RPE is confined to the underlying tissue layer.

Table 1 Central peak value of cross correlation between C-scans extracted at the posterior tips of the OS and retinal layers at four other depths (OPL, ELM, IS/OS junctions, and RPE). Central peak values are shown for four retinal eccentricities and two subjects. The absolute value of the cross correlation can range from zero to one.

Subject	Retinal layer	Retinal eccentricity			
		1°	2°	3°	7°
DTM	OPL	0.05	0.13	0.09	-
	ELM	0.08	0.12	0.09	-
	IS/OS	0.38	0.44	0.46	-
	RPE	0.09	0.12	0.07	-
RJ	OPL	0.10	0.07	0.06	0.05
	ELM	0.05	0.05	0.06	0.1
	IS/OS	0.30	0.31	0.47	0.47
	RPE	0.08	0.09	0.06	0.05

While the general finding is that bright reflections in cone photoreceptors occur near the IS/OS junctions and OS posterior tips, bright reflections were also observed within the OS of some, but not all, cones. These internal reflections are clearly visible in the Fig. 6 videos and are in stark contrast to the lack thereof in the inner segments, which appear uniformly dark in comparison. We have no reason to believe that the internal reflections are not real. It would be of interest to track the dynamics of these reflections over time, assess their dependence on photopigment bleaching, and quantify the extent to which they contribute to the overall waveguided light produced by the cones.

There have been several reports showing the primary benefits of adding AO to a SD-OCT retina camera are increased lateral resolution and increased SNR [12-14]. These reports have been based on evaluation of B-scan images of the retina or volume images that have been acquired over several seconds, a time frame that exposes the retinal image to significant retina motion blur and distortion. Our AO SD-OCT camera, on the other hand, rapidly acquires small volume images in a sufficiently short time period that motion artifacts are largely minimal. With motion artifacts greatly reduced and our camera's ability to image individual cone photoreceptors *en face*, we assessed whether the previously reported resolution and sensitivity increases are also apparent in C-scan images of single cone cells. Figure 11 illustrates our findings. Figures 11(a) and 11(b) show the same extracted C-scans of posterior tips of the OS, acquired with and without AO and from the same subject. In Fig. 11(a) the C-scans are mapped to their own gray scale so as to permit better visualization of the retinal structure in either image. The regular array of cone photoreceptors is readily evident in the C-scan image acquired with AO. A somewhat regular pattern with reduced contrast is partially visible in the image acquired without AO. While this pattern is probably related to the cone mosaic, clarity of the cones is noticeably reduced. Similar findings were observed at the other retinal eccentricities. In Fig. 11(b) the C-scans are mapped to the same gray scale, i.e., normalized to the brightest pixel from either C-scan. With this mapping, it is visually apparent that the C-scan acquired with AO is much brighter than the one acquired without. Quantitative analysis of the C-scans confirms that the SNR increased by 7 dB. Retinal images acquired from the other subject revealed a similar pattern with cone photoreceptors visible and an

increase in the SNR (8.2 dB) with AO. In general AO was necessary for observing individual cone photoreceptor cells and led to a significant increase in the SNR in C-scan images.
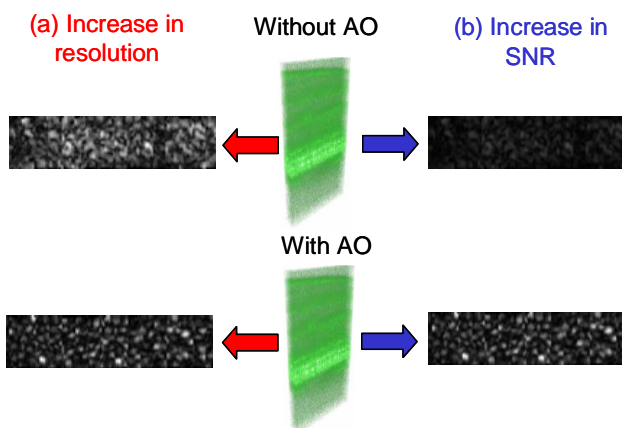

Fig. 11. Two primary benefits of correcting ocular aberrations across a large pupil in an OCT retina camera. (a) C-scan images at the posterior tips of the OS show an increase in lateral resolution with AO. The two images are normalized to their own gray scale so as to permit better visualization of the cone photoreceptor structure. (b) The same C-scan images in (a), but adjusted to the same gray scale. Note the increased brightness with AO. Both volume images (with and without AO) were acquired at essentially the same 2° retinal eccentricity. Focus is approximately at the plane of the photoreceptors. C-scans are displayed using a linear intensity scale; volume images are displayed using a log scale.

4. Conclusion

We demonstrate a fiber based AO spectral-domain OCT camera for imaging the living retina with high 3D resolution (3x3x4.8 μm) and speed (75,000 A-scan/s). The acquisition rate is more than two times faster than that previously reported in the literature. Unlike previous AO-OCT and AO-SLO instruments, the wavefront corrector of the AO was strategically positioned between the XY mechanical scanners and the subject's eye. This arrangement avoided possible beam distortion at the pupil plane, which was predicted for our original AO SD-OCT system design. Retina motion artifacts were minimized by quickly acquiring small volume images of the retina with and without AO compensation.

Initial results demonstrate a 7 to 8.2 dB increase in SNR of the photoreceptor layer with AO correction. Camera sensitivity was sufficient to detect reflections from all major retinal layers. The distribution of bright spots observed within C-scans at the IS/OS junctions and at the posterior tips of the OS were found to be significantly correlated to one another as well as to the expected cone spacing. No correlation was found between the posterior tips of the OS and the OPL, ELM, and RPE. This finding is strong evidence that the waveguided light that reflects back out of cone photoreceptors largely originates from only two narrow layers that straddle the OS in the retina. We found no evidence that the light reflected from the RPE was recaptured by the overlying cone photoreceptors.

Acknowledgments

performed under the auspices of the U.S. Department of Energy by University of California Lawrence Livermore National Laboratory under contract No. W-7405-Eng-48.